Magnetic states of iron-based two-leg ladder tellurides

Yang Zhang,[1,2] Ling-Fang Lin,[1,2] Adriana Moreo,[1,3] Shuai Dong,[2] and Elbio Dagotto[1,3,*]

[1] *Department of Physics and Astronomy, University of Tennessee, Knoxville, TN 37996, USA*
[2] *School of Physics, Southeast University, Nanjing 211189, China*
[3] *Materials Science and Technology Division, Oak Ridge National Laboratory, Oak Ridge, TN 37831, USA*

(Dated: September 2, 2019)

The recent discovery of superconductivity at high pressure in the two-leg ladder compounds $BaFe_2X_3$ (X=S, Se) started the novel field of quasi-one-dimensional iron-based superconductors. In this publication, we use Density Functional Theory (DFT) to predict that the previously barely explored ladder compound $RbFe_2Te_3$ should be magnetic with a CX-type arrangement involving ferromagnetic rungs and antiferromagnetic legs, at the realistic density of $n = 5.5$ electrons per iron. The magnetic state similarity with $BaFe_2S_3$ suggests that $RbFe_2Te_3$ could also become superconducting under pressure. Moreover, at $n = 6.0$ our DFT phase diagrams (with and without lattice tetramerization) reveal that the stable magnetic states could be either a 2×2 magnetic Block-type, as for X=Se, or a previously never observed before CY-type state, with ferromagnetic legs and antiferromagnetic rungs. In the Te-based studies, electrons are more localized than in S, implying that the degree of electronic correlation is enhanced for the Te case.

INTRODUCTION

Although the first high critical temperature iron-based superconductors were discovered more than a decade ago, the origin of its pairing mechanism is still highly debated and the topic remains one of the most important open problems in Condensed Matter Physics [1–4]. It is widely believed that the crystal structure, magnetic properties, and the degree of electronic correlation are all fundamental aspects to clarify the physics of these materials [2, 5–7]. For the vast majority of initially reported iron-based superconductors, the crystal structures consisted of slightly distorted two-dimensional (2D) iron square lattices made of FeX_4 tetrahedra (X = pnictides or chalcogens) [6, 8, 9]. The electronic correlation effects can not be neglected [4], causing many novel physical features, such as Fermi surfaces without hole pockets, complex magnetic spin orders, as well as orbital selective Mott states [2, 4].

Recently, the discovery of superconductivity in the so-called 123-type compounds $BaFe_2X_3$ (X=S/Se) opened a new branch of research in iron-based superconductors [10, 11]. Different from the 2D iron square lattice arrangement, the 123-type iron chalcogenides display a dominant quasi-one-dimensional two-leg ladder crystal structure that has been much analyzed [12–17]. These recent developments resemble the discovery in the 90's of superconductivity in Cu-oxide ladders [18–20] that opened a fertile area of research.

Under ambient conditions, $BaFe_2S_3$ displays CX stripe antiferromagnetic (AFM) order – AFM along the legs and ferromagnetic (FM) along the rungs – below 120 K with a magnetic moment $\sim$ 1.2 μ_B/Fe [10, 21]. This magnetic moment is smaller than the theoretical maximum value of 4 μ_B/Fe, obtained by considering the high-spin $S = 2$ configuration and the electronic density $n = 6.0$ for $BaFe_2S_3$. Superconductivity was observed at $P \sim 11$ GPa with the highest critical temperature T_C being 24 K [10, 22]. Since then, several experimental and theoretical studies have followed [23–27]. Above 10 GPa, a metal-insulator transition (MIT) and associated first-order magnetic phase transition were recently observed for $BaFe_2S_3$ [28, 29]. One possible explanation is that pressure changes the bandwidth of these materials, thus altering the degree of correlation [10, 11]. An alternative, based on model calculations, is that high pressure may change the Fe electronic density, effectively doping the two-leg ladders. In fact, calculations based on the density matrix renormalization group [30] observed clear tendencies to form Cooper pairs at intermediate Hubbard coupling strengths upon light doping. Similar self-doping effects under pressure were also obtained using DFT calculations [28].

$BaFe_2Se_3$ is another recently discovered superconducting ladder under high pressure [11]. Without external pressure, $BaFe_2Se_3$ is an AFM Mott insulator and displays an exotic Block-type magnetic order below $\sim$ 256 K, with a robust local magnetic moment $\sim$ 2.8 μ_B/Fe [12, 13, 31, 32]. This material is theoretically predicted to be multiferroic [16] and recently confirmed to be polar at high temperature [33]. In particular, $BaFe_2Se_3$ is in an orbital-selective Mott phase (OSMP) according to neutron experiments at ambient pressure [17]. Moreover, there are several other two-leg ladder iron chalcogenides, with almost all the studies focusing on iron sulfides and selenides. For example, KFe_2Se_3 was observed to have a CX-type stripe AFM order [31], similarly $CsFe_2Se_3$ [21] and $RbFe_2Se_3$ [23]. In particular, the KFe_2S_3 compound was predicted to display a first-order transition under high pressure in our recent work [28].

Considering the columns of pnictogens and chalcogens in the periodic table, the next natural step in iron ladders is to move one row down and use Sb or Te. However, surprisingly there is virtually no experimental lit-

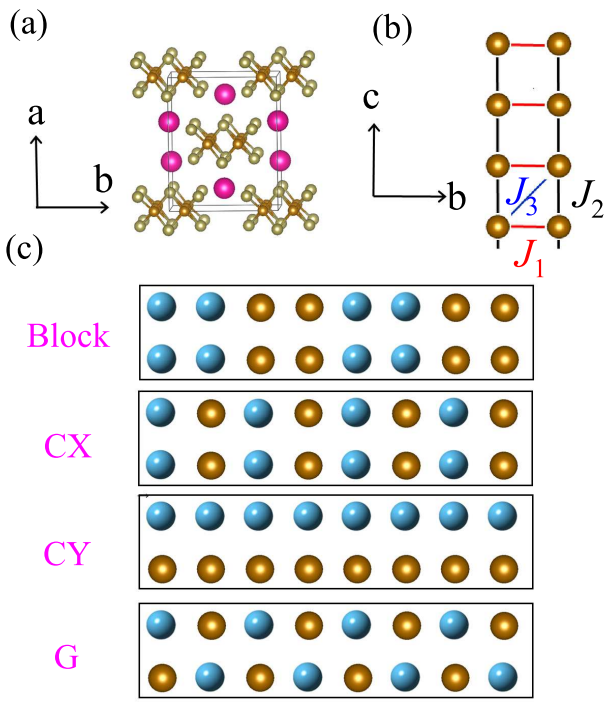

FIG. 1. (a) Schematic crystal structure of $RbFe_2Te_3$ (electronic density $n = 5.5$) with the convention: Pink = Rb; Brown = Fe; Dark Yellow = Te. (b) Sketch of one *Cmcm* ladder. The iron-iron distance is uniform along the legs. (c) Sketch of possible antiferromagnetic magnetic orders in each individual ladder. Spin up and spin down are distinguished by different colored balls.

erature available using these elements. For Te, we are only aware of *one* publication many years ago where it was reported that $RbFe_2Te_3$ also favors the *Cmcm* crystal structure [34], similar to $BaFe_2S_3$, where the iron-iron distances are uniform in the non-tilting ladder, as shown in Fig. 1. In $RbFe_2Te_3$, the valence of Fe is +2.5 indicating that the realistic density is $n = 5.5$ electrons per iron considering the $4s^2 3d^6$ configuration in the Fe atoms. It is important to remark that there are still no $n = 5.5$ ladders being reported to be superconducting under pressure. As already expressed, early work for $BaFe_2S_3$ considered that superconductivity under pressure was controlled by the bandwidth in a Mott transition. Moreover, pressure enhanced the hybridization between Fe $3d$ and S $3p$ orbitals [10, 29]. Due to the weaker electronegativity of Te atoms in chalcogenides, it is reasonable to assume that the Fe and Te atoms will be more hybridized providing convenient conditions for superconductivity.

In the present publication, the magnetic properties and electronic structure corresponding to $RbFe_2Te_3$ are studied based on first-principles DFT calculations. The CX-type spin order is predicted to be the most likely magnetic ground state in our $n = 5.5$ DFT phase diagrams. For comparison, for the $n = 6.0$ $BaFe_2Se_3$ compound the 2×2 magnetic Block-type state was found to be stable after including lattice tetramerization. In the Te-based compound, we found that electrons are more localized than in S, implying that the degree of electronic correlation is enhanced for the Te case. Future experimental efforts should be devoted to this interesting Te-ladder compound.

METHOD

The first-principles DFT calculations used here were performed with the projector augmented-wave (PAW) potentials as implemented in the Vienna *ab initio* Simulation Package (VASP) code [35, 36]. The Perdew-Burke-Ernzerhof (PBE) exchange function was employed [37] and the plane-wave cutoff energy was 500 eV. Since different magnetic configurations have different minimal unit cells, the mesh was appropriately modified for all the candidates to render the k-point densities approximately the same in reciprocal space, i.e. $6\times6\times8$ for Block-type and $6\times5\times10$ for FM-type. In addition, we have tested that these k-point meshes already lead to converged energies when compared with denser meshes.

As a first step, we considered the Local Spin Density approach (LSDA) with generalized gradient approximation (GGA) potential [37] to study the lattice ground-state properties of bulk $RbFe_2Te_3$. Since the PBE-GGA function is known to give an accurate description of the two-leg ladder systems [28, 38, 39], we do not consider the effective Hubbard $U_{\rm eff}$. Both the lattice constants and atomic positions were fully relaxed with different spin configurations until the force on each atom was below 0.005 eV/Å.

To understand magnetism, we adopted the Local Density approach (LDA) + U method [40], where the on-site Coulomb interaction U and on-site exchange interaction J were considered. To alleviate the computing time required, we just considered the $(0,0,0)$ order between ladders with minimum unit cell to obtain the phase diagram of the $n = 5.5$ and $n = 6.0$ ladders. Due to the dominance of the in-ladder magnetic order, the magnetic correlations between ladders can only slightly affect the energies and physical properties.

The generalized LDA+U functional is the following [40, 41]:

$$E^{\rm LDA+U}[\rho^\sigma(r),[\{n^\sigma\}] = E^{\rm LSDA}[\rho^\sigma(r)] + E^U[\{n^\sigma\}] - E_{\rm dc}[\{n^\sigma\}], \quad (1)$$

where $\rho^\sigma(r)$ is the charge density for electrons with spin projection σ, while $\{n^\sigma\}$ are the elements of the density matrix. Here, the density matrix is defined as:

$$n^\sigma_{mm'} = -1/\pi \int^{\rm E_F} ImG^\sigma_{ilm,ilm'}(E)dE, \quad (2)$$

where i denotes site, l indicates the orbital quantum number, and m the spin number. Note that there is summation for i and l implicit. Here, $G^{\sigma}_{ilm,ilm'}(E) =< ilm\sigma|(E-H)^{-1}|ilm'\sigma >$ are the matrix elements of the Green function matrix in the localized representation, and H is the effective single-electron Hamiltonian. The orbital polarizations are absence in the LSDA first term, and the second term in Eq.(1) can be described by the Hartee-Fock (HF) mean-field theory [40, 41]:

$$E^U[\{n\}] = 1/2 \sum_{\{m\},\sigma} \{< m,m''|V_{\rm ee}|m',m''' > n^{\sigma}_{mm'} n^{-\sigma}_{m''m'''} + (< m,m''|V_{\rm ee}|m',m''' > - < m,m''|V_{\rm ee}|m''',m' >) n^{\sigma}_{mm'} n^{\sigma}_{m''m'''}\}, \quad (3)$$

where $V_{\rm ee}$ are the screened Coulomb interactions among nl-electrons. The double counting term ($E_{\rm dc}$) is described by

$$E_{\rm dc}[\{n^{\sigma}\}] = 1/2Un(n-1) - 1/2J[n^{\uparrow}(n^{\uparrow}-1) + n^{\downarrow}(n^{\downarrow}-1)], \quad (4)$$

where $n^{\sigma} = Tr(n^{\sigma}_{mm'})$ and $n = n^{\uparrow} + n^{\downarrow}$. U and J are the Coulomb interaction and exchange interaction, respectively. If the density matrix becomes diagonal, the present rotationally-invariant method is equivalent to the ordinary LDA+U approach [42].

RESULTS

Physical properties of $RbFe_2Te_3$

To find out what magnetic configuration becomes the ground state of $RbFe_2Te_3$, we adopted the LSDA method with the GGA potential to fully relax the crystal lattices and atomic position since the PBE-GGA function was widely used in previous DFT calculations of two-leg iron ladder systems [26, 28, 38, 39]. Various possible (in-ladder) magnetic arrangements were imposed on the iron ladders [see Fig. 1(c)], such as non-magnetic (NM), FM, AFM with FM rungs and AFM legs (CX), AFM with AFM rungs and FM legs (CY), AFM in both rung and leg directions (G), and 2×2 Block-AFM (Block) [28]. Furthermore, the (π, π, 0) order between ladders was adopted, as suggested by neutron scattering results [31] for $K_xBa_{1-x}Fe_2Se_3$. Our main results for $RbFe_2Te_3$ are summarized in Table I.

Under ambient conditions, our DFT calculations performed for several magnetic candidates [the tested spin configurations are shown in Fig. 1(c)] indicate that the CX-type magnetic order is the most stable ground state of the ensemble used. For this CX-type state, the calculated local magnetic moment of Fe is about 2.71 $\mu_{\rm B}$/Fe. It should be noted that it is quite common to overestimate the local magnetic moment when using LSDA calculations of iron-based superconductors [5, 28, 39], which may be caused by the coexistence of localized Fe spins and itinerant electrons [43]. Another possibility is the existence of strong quantum zero-point fluctuations in this quasi-one-dimensional two-leg ladder system. For comparison, the calculated local magnetic moment for $BaFe_2S_3$ and KFe_2Se_3 are 2.08 $\mu_{\rm B}$/Fe [28, 39] and 2.65 $\mu_{\rm B}$/Fe [28], respectively, which is smaller than the experimental values 1.2 $\mu_{\rm B}$/Fe and 2.1 $\mu_{\rm B}$/Fe [10, 44]. Hence, it is reasonable to assume that the experimental magnetic moment would be smaller than our calculated value for $RbFe_2Te_3$.

TABLE I. The optimized lattice constants (Å), local magnetic moments (in $\mu_{\rm B}$/Fe units) within the default PAW sphere, and band gaps (eV) for the various magnetic configurations, as well as the energy differences (meV/Fe) with respect to the CX configuration taken as the reference of energy. The experimental values (Exp. for short) are also listed for comparison.

	$a/b/c$	M	Gap	Energy
NM	12.665/9.953/5.683	0	0	396
FM	13.164/10.625/5.629	2.64	0	238
CX	12.803/10.233/5.868	2.71	0.39	0
CY	12.622/10.522/5.653	2.43	0	236
G	12.771/10.326/5.795	2.54	0	90
Block	13.008/10.454/5.570	2.45	0	158
Exp.	12.486/10.126/5.921	–	–	–

The DFT calculated energy gap corresponding to the CX-type AFM order is about 0.39 eV, which is close to the activation gap reported for $CsFe_2Se_3$ [14]. This calculated $RbFe_2Te_3$ gap is larger than the experimental value of $BaFe_2S_3 \sim 0.06 - 0.07$ eV [56]. According to the empirical knowledge gathered on iron-ladders, the larger gap indicates that a much higher pressure will be needed in the Te case to achieve an insulator-metal transition or to suppress magnetism, than in the S or Se cases.

Considering the intra-ladder magnetic order, the magnetism of $RbFe_2Te_3$ could be described by a simple Heisenberg model:

$$H_{\rm spin} = -J_1 \sum_{<i,j>} \mathbf{S}_i \cdot \mathbf{S}_j - J_2 \sum_{[k,l]} \mathbf{S}_k \cdot \mathbf{S}_l - J_3 \sum_{\{m,n\}} \mathbf{S}_m \cdot \mathbf{S}_n, \quad (5)$$

where J_1 and J_2 are the exchange interactions in the rung and leg directions, respectively, while J_3 is the exchange coupling along the plaquette diagonal of iron atoms. By fitting the DFT energies of various magnetic states, all the coefficients of this Heisenberg model can be obtained: $S^2J_1 = 44.2$ meV, $S^2J_2 = -96.1$ meV, and $S^2J_3 = -23.1$ meV, respectively [45]. Similar to two-dimensional magnetic stripe iron superconductors and other two-leg iron ladders [3, 23, 46], they all display that the magnitude of the FM rung exchange coupling is smaller than the magnitude of the AFM leg coupling.

According to the calculated density of states (DOS)

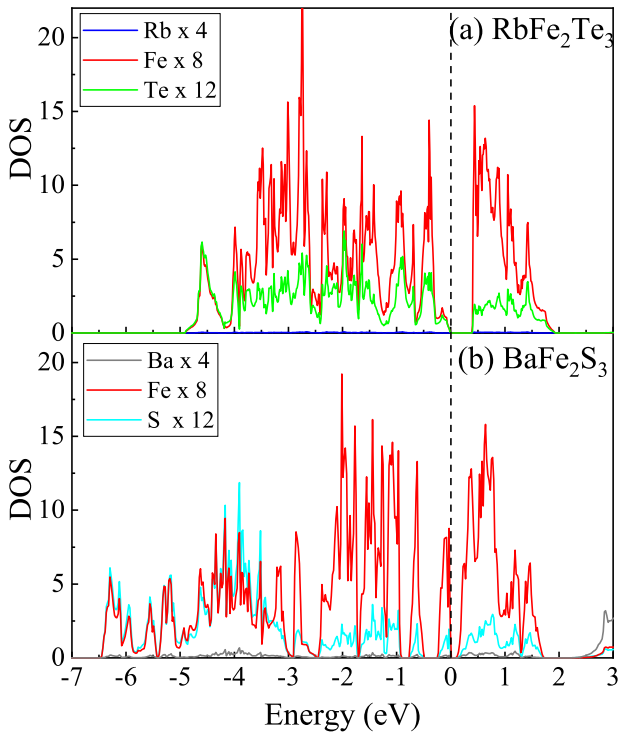

FIG. 2. DOS near the Fermi level using the CX-AFM states (π, π, 0) for (a) $RbFe_2Te_3$ (at electronic density $n = 5.5$) and $BaFe_2S_3$ (at electronic density $n = 6.0$), respectively. Blue= Rb; Black = Ba; Red = Fe; Green = Te; Cyan = S.

of the CX-type AFM order of $RbFe_2Te_3$ [see Fig. 2(a)], the bands near the Fermi level are mainly contributed by Fe-3*d* orbitals which are highly *hybridized* with Te-5*p* orbitals. For comparison, we displayed the DOS of the CX-type AFM state of $BaFe_2S_3$ in Fig. 2(b). It is clearly shown that the bandwidth of the five iron bands of $RbFe_2Te_3$ ($\sim$ 6.8 eV) is smaller than $BaFe_2S_3$ ($\sim$ 8 eV), which indicates the iron orbitals of $RbFe_2Te_3$ are more localized than in $BaFe_2S_3$.

It is interesting that the weight of Fe and Te near the Fermi level are smaller than in the case Fe and S. One possible reason is that $RbFe_2Te_3$ has 0.5 electrons less than $BaFe_2S_3$ per iron ion, resulting in fewer iron states in $RbFe_2Te_3$. Another possible reason maybe a stronger covalent bond behavior between Fe and Te. Considering the electronegativity of chalcogens, the covalent bond behavior would increase from S to Te. This tendency was supported by previous DFT calculations for $BaFe_2Se_3$ [16]. This covalent bond behavior also will enhance the hybridization between the Fe 3*d* orbitals and Te 5*p* orbitals, resulting in an increase at the Fermi level of the weight of Te.

Magnetic phase diagrams for two-leg ladders at electronic densities $n = 5.5$ and $n = 6.0$

To understand better the magnetic properties of two-leg iron ladders, we used the LDA+U method with GGA potential to compare different spin configurations by changing the on-site Coulomb interaction U and on-site exchange interaction J. Here, to save computing resources, the (0, 0, 0) order between ladders was considered because the in-ladder magnetic coupling is dominant in two-leg iron systems.

Let us start our description of the main results considering the ladder electronic density $n = 5.5$, corresponding to $RbFe_2Te_3$, using periodic boundary conditions, based on the experimental crystal structure [34]. As shown in Fig. 3(a), there is only one magnetic state (CX-type) stable in our phase diagram [except for one point ($U = 1.5$ eV and $J/U = 0.15$)] when the Hubbard coupling U and exchange interaction J are varied in a wide range. This clearly indicates that the CX-type order is quite stable in our $n = 5.5$ phase diagram, which is consistent with existing studies of magnetism in $n = 5.5$ iron ladders [10, 23, 31]. Hence, we can arrive to the reasonable conclusion that the CX-type AFM is most likely the magnetic ground state of other iron ladders with electronic density $n = 5.5$. This CX state of iron ladders can be considered quite similar to the prevalent stripe C-AFM order of iron 2D layered systems [4, 47, 48].

To qualitatively describe the Mott insulator of $RbFe_2Te_3$, we calculated the magnetic moment and energy gap by increasing U at the realistic $J/U = 0.25$ [4], as displayed in Fig. 3(b). When U is small, the magnetic moment of iron is zero, all the iron bands overlap, and the system is in a metallic state. By increasing U to a critical value, the spin up and down bands split, resulting in the CX-type AFM order while the system is still metallic in a very narrow U range near 1.25 eV. Continuing to increase U, the valence band and the conduction band separate from each other opening a gap, and producing an insulating phase. Our results for $J/U = 0.25$ qualitatively describe the Mott metal-insulator phase transition. In our LDA+U approximation, the Hubbard U splits the the spin up/down near $U = 1.2$ eV, and opens the gap at $U = 1.4$ eV.

Let us consider now the results for ladders with electronic density $n = 6.0$, corresponding to $BaFe_2Se_3$, which experimentally is known to display the exotic 2×2 Block-type AFM order [31]. As a first step, we use the crystal structure *without* lattice tetramerization. The phase diagram that we obtained for $n = 6.0$ iron ladders become far richer than at $n = 5.5$, as displayed in Fig. 4(a), including five different magnetic states, with a surprising dominance of the CY state, followed by CX with regards to area covered in the phase diagram [49]. Note that here there is only a small region of Block-type order displaying in our DFT phase diagram. However, it

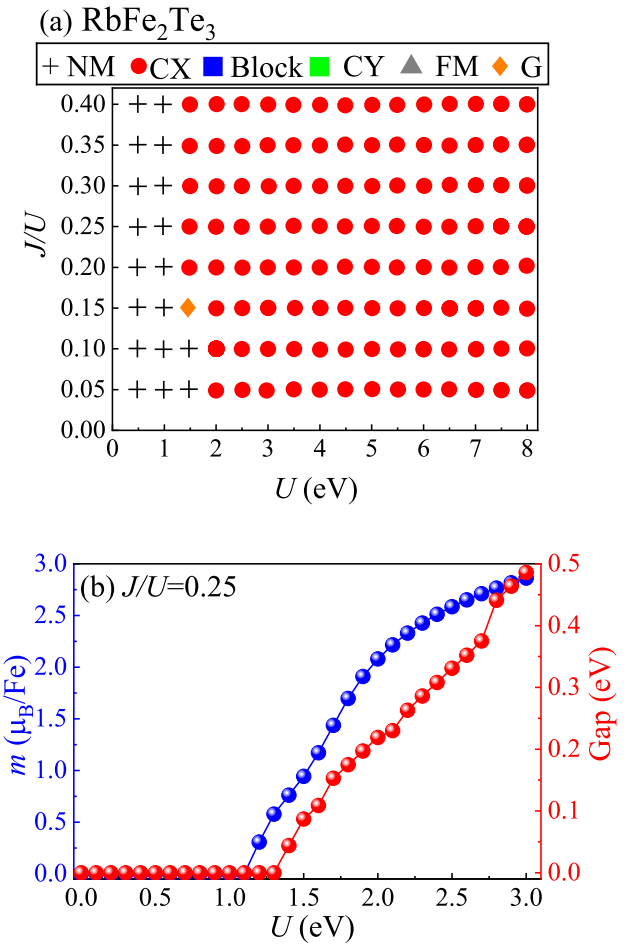

FIG. 3. (a) Phase diagram based on the experimental lattice constants of $RbFe_2Te_3$, employing the LDA+U technique at the electronic density $n = 5.5$. (b) Evolution of local magnetic moments and band gaps of $RbFe_2Te_3$ for the CX-type AFM magnetic state, as a function of U, at $J/U = 0.25$.

should remarked that the energy between Block-type and CY-type is less than 10 meV/Fe at $U = 3$ eV and 3.5 eV. In other regions of our phase diagram, the energy of Block-type remains only slightly higher than the energy of CY-type. To address better this issue note that the Block-type AFM order naturally brings up the issue of exchange magnetostriction related to a possible lattice tetramerization induced by this Block order, which would reduce the overall energy. Hence, the Block-type order may become more stable than the CY-type in some region by considering the lattice tetramerization. Moreover, according to related DFT calculations and actual experiments [16, 33, 38], the symmetry of the crystal structure of $BaFe_2Se_3$ is reduced due to intra- and inter-ladder lattice distortions.

Thus, next we *include* the lattice tetramerization in our calculations. By comparing the energies with different magnetic orders we obtain the new phase diagram shown now in Fig. 4(b). The previously remarked small

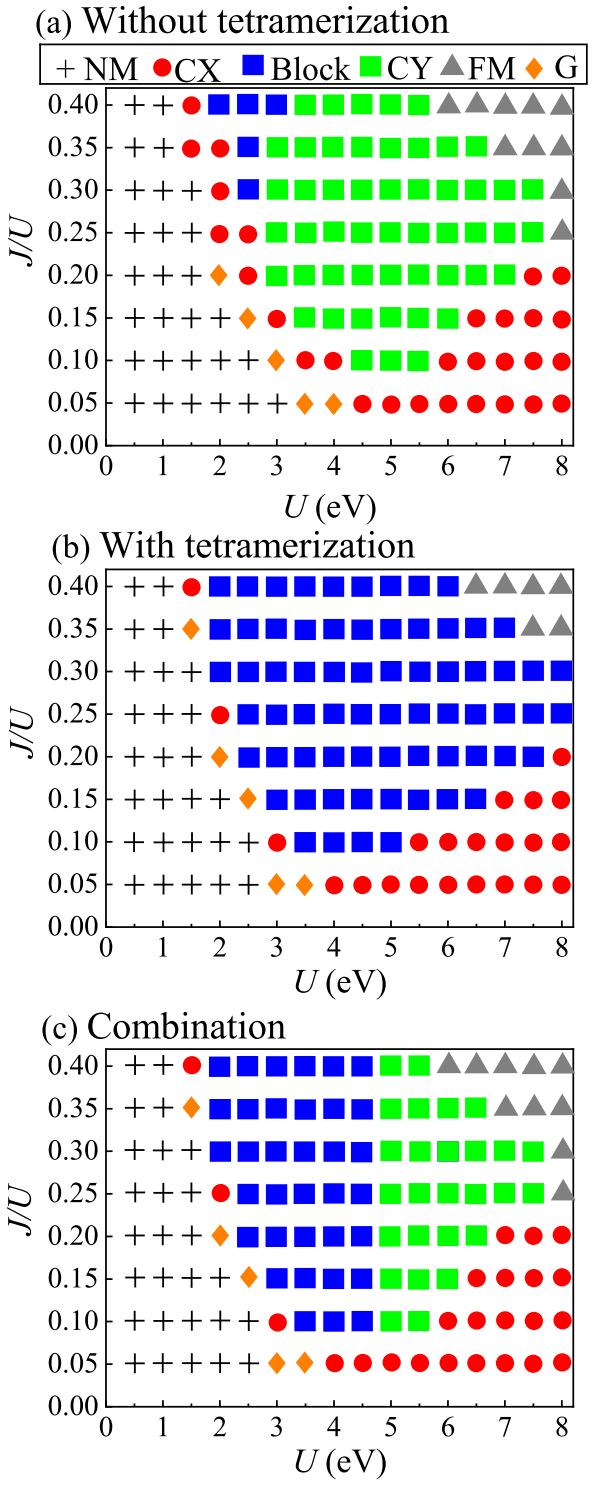

FIG. 4. (a-c) Phase diagrams of $BaFe_2Se_3$, employing the LDA+U technique with electronic density $n = 6.0$. (a) Without tetramerization. (b) With tetramerization. (c) Combination, which is the most reliable prediction, obtained by comparing energies with and without tetramerization.

energy difference favoring CY over Block states is now reversed in order, and in the new phase diagram with tetramerization, the CY-type AFM state does not appear in the whole $U - J$ plane. Instead, the Block-type state becomes more stable because its energy naturally decreases due to the tetramerization. However, it should be noted that the energies of other magnetic orders increase due to the reduced symmetry. In fact, different magnetic orders have different favorable symmetries. Therefore, it is natural that the phase diagram has changed so dramatically by considering the lattice tetramerization.

As a consequence, the best procedure to arrive to our final result is to compare the data of the different magnetic states with and without the lattice tetramerization. The resulting "combined" phase diagram is presented in Fig. 4(c). In fact, the best methodology is to fully optimize the crystal for each different magnetic orders with various J and U, but this is a formidable task. Here, we simply calculated the energies of Block-type AFM states with lattice tetramerization, and compared against the energies of other magnetic configurations without lattice tetramerization. As shown in Fig. 4(c), the CY-type becomes stable in some portions of the phase diagram. For the widely used before $J/U = 0.25$, the qualitative tendency with increasing U is first to form a CX-type AFM in a narrow region, followed by a robust Block-type AFM area, and then another robust CY-type AFM region, finally arriving to FM order with further increasing U [50] Qualitatively, the proliferation of many competing states at $n = 6.0$ as compared with $n = 5.5$ probably arises from a combination of correlation effects, increasing Hubbard U and decreasing bandwidth, as well as spin frustrating tendencies between the fully FM state in one extreme and the purely AFM state (in small regions) in the other, as discussed in previous Hartree Fock calculations [15]. In summary, it can be reasonably assumed that the magnetic state of the $n = 6.0$ Te-based iron ladders, if ever prepared experimentally, will not be the CX-type AFM but more likely either the Block- or CY-type arrangements.

Projected band structure and density of state

In Fig. 5, we present the projected band structure of the non-magnetic states for the five iron $3d$ orbitals corresponding to $RbFe_2Te_3$ and $BaFe_2S_3$, respectively. It is shown that the band structure is dispersive from Γ to Z, which is indicative of the quasi-one-dimensional behavior along the k_z axis. We observed that the full bandwidth of the five iron $3d$ orbitals of $RbFe_2Te_3$ is smaller than for the case of $BaFe_2S_3$, which suggests that the electrons of $RbFe_2Te_3$ are more localized than in $BaFe_2S_3$. In fact in our calculations, the bandwidth of the $3d$ orbitals for $RbFe_2Te_3$ and $BaFe_2S_3$ are about 3.56 eV and 4.06 eV, respectively. In addition, there are 0.5 electrons per Fe

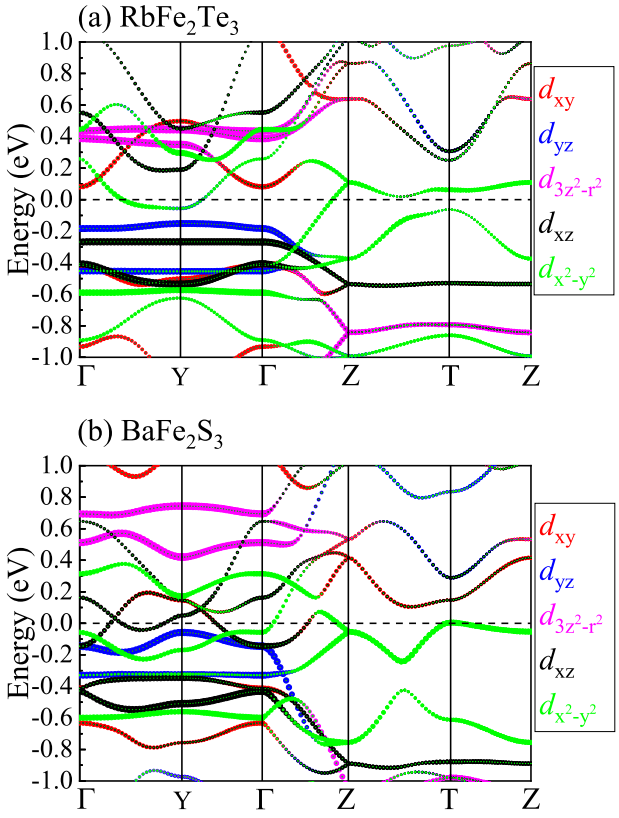

FIG. 5. Projected band structures of $RbFe_2Te_3$ (electronic density $n = 5.5$) and $BaFe_2S_3$ (electronic density $n = 6.0$) for the non-magnetic (NM) state, respectively. The Fermi level is shown with dashed lines. The weight of each iron orbital is represented by the size of the circle.

less in $RbFe_2Te_3$ than in $BaFe_2S_3$. In $RbFe_2Te_3$, the Fermi surface is mainly contributed by the $d_{x^2-y^2}$ orbital and the contribution of the d_{yz} is reduced, as shown in Fig. 5(a). In fact, the d_{yz} orbital crosses the Fermi level along the Y to Γ and Γ to Z paths, but it is hybridized with the $d_{x^2-y^2}$ orbital. For comparison, in $BaFe_2S_3$, the Fermi pockets are mainly contributed by the $d_{x^2-y^2}$, d_{xy}, and d_{xz} orbitals as displayed in Fig. 5(b). This suggests that the Fermi pockets of $RbFe_2Te_3$ are different from $BaFe_2S_3$.

According to the DOS [see Fig. 6], we calculated the relative proportion of the Fermi surface for the Te-ladder associated with each of the five iron orbitals: 64% are contributed by $d_{x^2-y^2}$ and 26% are from d_{yz}. In this context, it seems reasonable to assume that $RbFe_2Te_3$ can be described by a two orbital model or even just one with a combined orbital description ($d_{x^2-y^2}$ hybridized with d_{yz}). The pressure effect could likely shift the Fermi level and slightly change the electronic structure. The d_{xy} and d_{xz} DOS peaks may also shift to the Fermi level under pressure, which may reconstruct the Fermi surface. This requires more theoretical calculations and high pressure

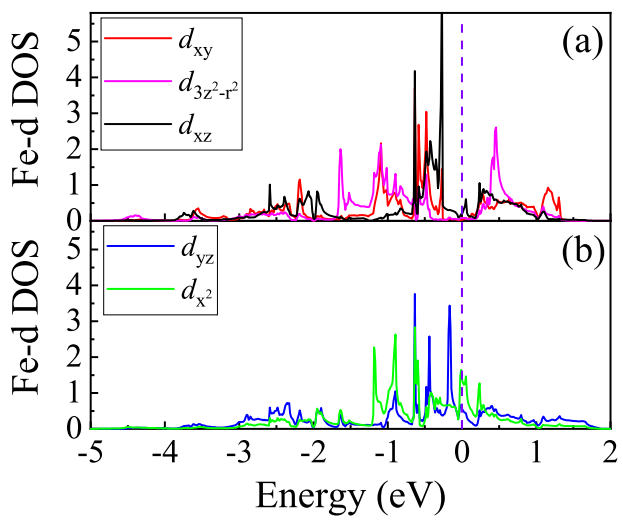

FIG. 6. The projected density of states of the Fe-d orbitals for the non-magnetic state of $RbFe_2Te_3$ (electronic density $n = 5.5$). The five iron $3d$ orbitals are distinguished by different colors.

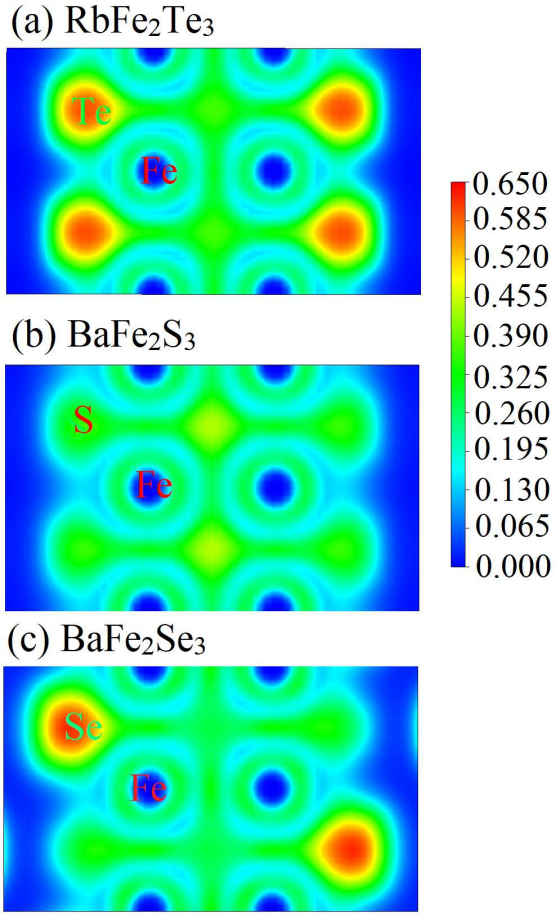

FIG. 7. The calculated electron localization function in the iron ladder plane for (a) $RbFe_2Te_3$, (b) $BaFe_2S_3$, and (c) $BaFe_2Se_3$, respectively. To better understand the localization of iron ladders, we set the range of ELF from 0 to 0.65. Generally, ELF=0 indicates no electron localization and ELF=1 indicates full electron localization.

experimental results to clarify better.

The $d_{3z^2-r^2}$ orbital does not contribute to the low-energy state suggesting that $d_{3z^2-r^2}$ may not play a crucial role for superconductivity in iron ladders. Since the superconducting phase dome of $BaFe_2S_3$ is in the vicinity to the CX-AFM region, the driving force of superconductivity may be mediated by spin fluctuations in the nonmagnetic state. According to our previous results of $n = 5.5$ pressured iron ladders [28], the NM phase can be found at high pressure. In this scenario, it is reasonable to assume that $RbFe_2Te_3$ may also become superconducting at high pressure due to the magnetic similarity, dominated by the CX state.

DISCUSSION

Both experimental and first-principles theoretical results revealed a clear tendency for the bandwidths W of the iron $3d$ orbitals to be enlarged under pressure in $BaFe_2X_3$ [10, 38, 51], thus enhancing the itinerant nature of the $3d$ iron electrons. Thus, in this respect pressure reduces the electronic correlation strength given by the ratio U/W. To better understand the electronic correlations of $RbFe_2Te_3$, we calculated the "electron localization function" (ELF) [52], widely used within *ab initio* methods to characterize the electron localization. As shown in Figs. 7(a) and (b), the electrons of $RbFe_2Te_3$ are more localized than in $BaFe_2S_3$, implying that the electronic correlation of Te-based ladders is stronger. Considering also the ELF of $BaFe_2Se_3$ [see Fig. 7(c)], which displays Block-type AFM order that is believed to originate in an orbital selective Mott state induced by electronic correlations [53–55], it is reasonable to conclude that the electronic correlation would be stronger than in $BaFe_2S_3$ as well, showing that the reasoning is self-consistent. The stronger electronic correlation unveiled in Te ladders are expected to create more interesting physical properties due to the competition of many degrees of freedom. However, it should be noted that there are no experimental studies available for $n = 6.0$ Te-based iron ladders, to our knowledge.

CONCLUSION

In this work, the two-leg iron ladder compound $RbFe_2Te_3$, with the iron density $n = 5.5$, was system-

atically studied using first-principles calculations. The CX-type state was predicted to be the most likely magnetic ground state. The bandwidths of the iron $3d$ bands in the case of $RbFe_2Te_3$ are smaller than in $BaFe_2S_3$. In addition, the phase diagram of ladders at electronic iron density $n = 6.0$, corresponding to $BaFe_2Se_3$, is found to be much richer than for $n = 5.5$. In particular, the 2×2 magnetic Block-type state could be stable at $n = 6.0$ according to DFT phase diagrams, particularly due to lattice tetramerization. Also the exotic CY state, with AFM rungs and FM legs, which has *not* been observed before neither in experiments nor in model calculations, has a large area of stability in the DFT phase diagram at $n = 6.0$.

In addition, considering the magnetic state similarity and electronic structure with other iron ladders, $RbFe_2Te_3$ may become superconducting under higher presure. Moreover, according to our ELF analysis, the electrons of Te-123 are more localized than in S, implying that the degree of electronic correlation is enhanced for the Te case. The potential relevance of strong correlation in Te-123 ladders may also induce exotic phenonema as the "orbital selective Mott physics" recently discussed using multiorbital Hubbard models [53–55]. Our overarching conclusion is that experimental studies of iron ladders using Te may lead to interesting results, such as exotic magnetic states and superconductivity under high pressure.

E.D. and A.M. are supported by the U.S. Department of Energy (DOE), Office of Science, Basic Energy Sciences (BES), Materials Sciences and Engineering Division. S.D., Y.Z., and L.F.L. were supported by the National Natural Science Foundation of China (Grant Nos. 11834002 and 11674055). L.F.L. and Y.Z. were supported by the China Scholarship Council. Y.Z. was also supported by the Scientific Research Foundation of Graduate School of Southeast University. Most calculations were carried out at the Advanced Computing Facility (ACF) of the University of Tennessee Knoxville (UTK).

* Corresponding author: edagotto@utk.edu

[1] G. R. Stewart, Rev. Mod. Phys. **83**, 1589 (2011).
[2] E. Dagotto, Rev. Mod. Phys. **85**, 849 (2013).
[3] P. C. Dai, Rev. Mod. Phys. **87**, 855 (2015).
[4] P. C. Dai, J. P. Hu, and E. Dagotto, Nat. Phys. **8**, 709 (2012).
[5] I. I. Mazin and M. D. Johannes, Nat. Phys. **5**, 141 (2009).
[6] D. C. Johnston, Adv. Phys. **59**, 803 (2010).
[7] Q. M. Si, R. Yu, and E. Abrahams, Nat. Rev. Mater. **1**, 16017 (2016).
[8] W. Li, H. Ding, P. Deng, K. Chang, C. L. Song, K. He, L. L. Wang, X. C. Ma, J. P. Hu, X. Chen, and Q. K. Xue, Nat. Phys. **8**, 126 (2012).
[9] W. Bao, Q. Z. Huang, G. F. Chen, M. A. Green, D. M. Wang, J. B. He, and Y. M. Qiu, Chin. Phys. Lett. **28**, 086104 (2011).
[10] H. Takahashi, A. Sugimoto, Y. Nambu, T. Yamauchi, Y. Hirata, T. Kawakami, M. Avdeev, K. Matsubayashi, F. Du, C. Kawashima, H. Soeda, S. Nakano, Y. Uwatoko, Y. Ueda, T. J. Sato and K. Ohgushi, Nat. Mater. **14**, 1008 (2015).
[11] J.-J. Ying, H. C. Lei, C. Petrovic, Y.-M. Xiao and V.-V. Struzhkin, Phys. Rev. B **95**, 241109(R) (2017).
[12] B. Saparov, S. Calder, B. Sipos, H. B. Cao, S. X. Chi, D. J. Singh, A. D. Christianson, M. D. Lumsden and A. S. Sefat, Phys. Rev. B. **84**, 245132 (2011).
[13] H. Lei, H. Ryu, A. I. Frenkel and C. Petrovic, Phys. Rev. B. **84**, 214511 (2011).
[14] F. Du, K. Ohgushi, Y. Nambu, T. Kawakami, M. Avdeev, Y. Hirata, Y. Watanabe, T. J. Sato, and Y. Ueda, Phys. Rev. B. **85**, 214436 (2012).
[15] Q. Luo, A. Nicholson, J. Rincón, S. Liang, J. Riera, G. Alvarez, L. Wang, W. Ku, G. D. Samolyuk, A. Moreo, and E. Dagotto, Phys. Rev. B. **87**, 024404 (2013).
[16] S. Dong, J. M. Liu, and E. Dagotto, Phys. Rev. Lett. **113**, 187204 (2014).
[17] M. Mourigal, Shan Wu, M.-B. Stone, J.-R. Neilson, J.-M. Caron, T.-M. McQueen, and C.-L. Broholm, Phys. Rev. Lett. **115**, 047401 (2015).
[18] E. Dagotto, J. Riera, and D. Scalapino, Phys. Rev. B **45**, 5744(R) (1992).
[19] E. Dagotto and T. M. Rice, Science **271**, 618 (1996). See also E. Dagotto, Rep. Prog. Phys. **62**, 1525 (1999).
[20] M. Uehara, T. Nagata, J. Akimitsu, H. Takahashi, N. Mori, and K. Kinoshita, J. Phys. Soc. Jpn. **65**, 2764 (1996).
[21] S. X. Chi, Y. Uwatoko, H. B. Cao, Y. Hirata, K. Hashizume, T. Aoyama, and K. Ohgushi, Phys. Rev. Lett. **117**, 047003 (2016).
[22] T. Yamauchi, Y. Hirata, Y. Ueda, and K. Ohgushi, Phys. Rev. Lett. **115** 246402 (2015).
[23] M. Wang, M. Yi, S. J. Jin, H. C. Jiang, Y. Song, H. Q. Luo, A. D. Christianson, C. de la Cruz, E. Bourret-Courchesne, D. X. Yao, D. H. Lee, and R. J. Birgeneau, Phys. Rev. B **94**, 041111(R) (2016).
[24] N. D. Patel, A. Nocera, G. Alvarez, A. Moreo, and E. Dagotto, Phys. Rev. B **96**, 024520 (2017).
[25] J. M. Pizarro and E. Bascones, Phys. Rev. Mater. **3**, 014801 (2019).
[26] L. Zheng, B. A. Frandsen, C. Wu, M. Yi, S. Wu, Q. Huang, E. Bourret-Courchesne, G. Simutis, R. Khasanov, D.-X. Yao, M. Wang, and R. J. Birgeneau, Phys. Rev. B **98**, 180402(R) (2018).
[27] E. J. König, A. M. Tsvelik, and P. Coleman, Phys. Rev. B **98**, 184517 (2018).
[28] Y. Zhang, L. F. Lin, J. J. Zhang, E. Dagotto, and S. Dong, Phys. Rev. B **95**, 115154 (2017).
[29] P. Materne, W. Bi, J. Zhao, M. Y. Hu, M. L. Amigó, S. Seiro, S. Aswartham, B. Büchner, and E. E. Alp, Phys. Rev. B **99**, 020505(R) (2019).
[30] N. D. Patel, A. Nocera, G. Alvarez, R. Arita, A. Moreo, and E. Dagotto, Phys. Rev. B **94**, 075119 (2016).
[31] J. M. Caron, J. R. Neilson, D. C. Miller, K. Arpino, A. Llobet, and T. M. McQueen, Phys. Rev. B **85**, 180405(R) (2012).
[32] Y. Nambu, K. Ohgushi, S. Suzuki, F. Du, M. Avdeev, Y. Uwatoko, K. Munakata, H. Fukazawa, S. X. Chi, Y. Ueda, and T. J. Sato, Phys. Rev. B **85**, 064413 (2012).
[33] T. Aoyama, S. Imaizumi, T. Togashi, Y. Sato, K.

Hashizume, Y. Nambu, Y. Hirata, M. Matsubara, and K. Ohgushi, Phys. Rev. B **99**, 241109(R) (2019).
[34] K.O. Klepp, W. Sparlinek, and H. Boller, J. Alloy. Compd. **238**, 1-5 (1996).
[35] G. Kresse and J. Hafner, Phys. Rev. B **47**, 558 (1993).
[36] G. Kresse and J. Furthmüller, Phys. Rev. B **54**, 11169 (1996).
[37] J. P. Perdew, K. Burke, and M. Ernzerhof, Phys. Rev. Lett. **77**, 3865 (1996).
[38] Y. Zhang, L. F. Lin, J. J. Zhang, E. Dagotto, and S. Dong, Phys. Rev. B **97**, 045119 (2018).
[39] M. T. Suzuki, R. Arita and H. Ikeda, Phys. Rev. B **92**, 085116 (2015).
[40] A. I. Liechtenstein, V. I. Anisimov, and J. Zaanen, Phys. Rev. B **52**, R5467(R) (1995).
[41] V. I. Anisimov, F. Aryasetiawan, and A. I. Liechtenstein, J. Phys.: Condens. Matter **9**, 767 (1997).
[42] V. I. Anisimov, J. Zaanen, and Ole K. Andersen, Phys. Rev. B **44**, 943 (1991).
[43] D. Ootsuki, N. L. Saini, F. Du, Y. Hirata, K. Ohgushi, Y. Ueda, and T. Mizokawa, Phys. Rev. B **91**, 014505 (2015).
[44] J. M. Caron, J. R. Neilson, D. C. Miller, A. Llobet, and T. M. McQueen, Phys. Rev. B **84**, 180409(R) (2011).
[45] Here, we qualitatively obtained the Heisenberg exchange couplings J by comparing the energies of several collinear magnetic orders. Choosing different sets of various magnetic states will result in different values of J. However, it will not change the qualitative tendencies.
[46] L. W. Harriger, H. Q. Luo, M. S. Liu, C. Frost, J. P. Hu, M. R. Norman, and P.C. Dai, Phys. Rev. B **84**, 054544 (2011).
[47] Y. Zhang, L.-F. Lin, J.-J Zhang, X. Huang, M. An, and S. Dong, Phys. Rev. Mater. **1**, 034406 (2017).
[48] K. Sasmal, B. Lv, B. Lorenz, A. M. Guloy, F. Chen, Y. Y. Xue, and C. W. Chu, Phys. Rev. Lett. **101**, 107007 (2008).
[49] In model calculations, there is a third coupling called U' representing the repulsion between electrons at different orbitals in the same atom. Rotational invariance imposes a constraint $U{=}U'{+}2J_H$ between the on-site same-orbital Hubbard U, the model Hund coupling J_H, and U' [30]. This restricts the range of J_H/U to be less than 1/3, otherwise if larger than 1/3 then $U' < J_H$ considered unphysical. Here, we include $J/U > 1/3$ for completeness, but none of our physical conclusions change if only $J/U < 1/3$ is studied.
[50] Ferromagnetic tendencies are natural in multiorbital systems with a large Hund coupling as found in [15] using Hartree Fock for iron ladders, in one dimensional $t-J$ systems for spins larger than 1/2 such as in J. Riera, K. Hallberg, and E. Dagotto, Phys. Rev. Lett. **79**, 713 (1997), and in double-exchange models for manganites.
[51] R. Arita, H. Ikeda, S. Sakai, and M.-To Suzuki, Phys. Rev. B **92**, 054515 (2015).
[52] A. Savin, O. Jepsen, J. Flad, O.-K. Andersen, H. Preuss, and H. G. von Schnering, Angew. Chem. Int. Ed. **32**, 187 (1992).
[53] J. Herbrych, N. Kaushal, A. Nocera, G. Alvarez, A. Moreo, and E. Dagotto, Nat. Comm. **9**, 3736 (2018), and references therein.
[54] N. D. Patel, A. Nocera, G. Alvarez, A. Moreo, S. Johnston, and E. Dagotto, Commun. Phys. **2**, 64 (2019).
[55] J. Herbrych, J. Heverhagen, N. D. Patel, G. Alvarez, M. Daghofer, A. Moreo, and E. Dagotto, Phys. Rev. Lett. **123**, 027203 (2019).
[56] Z. S. Gönen, P. Fournier, V. Smolyaninova, R. Greene, F. M. Araujo-Moreira, B. Eichhorn, Chem. Mater. **12**, 3331 (2000).